

Ultrasonic power transfer from a spherical acoustic wave source to a free-free piezoelectric receiver: Modeling and experiment

S. Shahab, M. Gray, and A. Erturk^{a)}

G. W. Woodruff School of Mechanical Engineering, Georgia Institute of Technology, Atlanta, Georgia 30332, USA

(Received 9 December 2014; accepted 24 February 2015; published online 13 March 2015)

Contactless powering of small electronic components has lately received growing attention for wireless applications in which battery replacement or tethered charging is undesired or simply impossible, and ambient energy harvesting is not a viable solution. As an alternative to well-studied methods of contactless energy transfer, such as the inductive coupling method, the use of ultrasonic waves transmitted and received by piezoelectric devices enables larger power transmission distances, which is critical especially for deep-implanted electronic devices. Moreover, energy transfer by means of acoustic waves is well suited in situations where no electromagnetic fields are allowed. The limited literature of ultrasonic acoustic energy transfer is mainly centered on proof-of-concept experiments demonstrating the feasibility of this method, lacking experimentally validated modeling efforts for the resulting multiphysics problem that couples the source and receiver dynamics with domain acoustics. In this work, we present fully coupled analytical, numerical, and experimental multiphysics investigations for ultrasonic acoustic energy transfer from a spherical wave source to a piezoelectric receiver bar that operates in the 33-mode of piezoelectricity. The fluid-loaded piezoelectric receiver under free-free mechanical boundary conditions is shunted to an electrical load for quantifying the electrical power output for a given acoustic source strength of the transmitter. The analytical acoustic-piezoelectric structure interaction modeling framework is validated experimentally, and the effects of system parameters are reported along with optimal electrical loading and frequency conditions of the receiver. © 2015 AIP Publishing LLC.

[<http://dx.doi.org/10.1063/1.4914130>]

I. INTRODUCTION

The transformation of ambient vibrations into low-power electricity for use in wireless electronic components has been heavily researched over the last decade under the broad field of energy harvesting.^{1–13} There are other scenarios in which an electronic component has little or no ambient vibrational energy available to harvest; yet the wireless charging of its battery is of great need and interest. Example applications range from medical implants to sensors located in hazardous or inaccessible environments. Research efforts presented to address this challenge in the field of Contactless Energy Transfer (CET) have received uniformly growing attention.^{14–22} The most popular CET method, inductive coupling,^{14–17} has various drawbacks such as limited distance of efficient power transfer²⁰ (typically on the order of transmitter/receiver size), high conduction losses due to large reactive current needs, high switching losses in power electronics due to typical high frequencies, and the necessary involvement of electromagnetic fields (which may not be allowed in certain applications). Recently, Ultrasonic Acoustic Energy Transfer (UAET) has been suggested as an alternative CET method to overcome these issues. UAET has the potential to provide larger power transfer distances employing smaller transmitter/receiver dimensions, while using frequency ranges with minimal associated electronic or propagation losses. Additionally, UAET is

well suited in applications where electromagnetic fields are not allowed.¹⁸

A brief review of the limited and mostly experimental literature of UAET provides examples of proof-of-concept demonstrations. After the early work by Cochran *et al.*^{23,24} who suggested stimulation of osteogenesis by UAET, Kawanabe *et al.*²⁵ and Suzuki *et al.*²⁶ proposed methods for combined delivery of power and information to implanted medical devices. Recently, Ozeri and Shmilovitz¹⁹ investigated an ultrasonic transcutaneous energy transfer method for powering implanted devices, numerically and experimentally. They¹⁹ presented optimized designs of two ultrasonic piezoelectric disk transducers used as the transmitter external to the body and receiver implanted inside the body. More recently, Maleki *et al.*²⁷ presented a method to transmit ultrasonic wave power to an implantable micro-oxygen generator with less directionality and greater power transmission efficiencies. It is worth mentioning that UAET is better suited for media with specific impedance similar to that of the respective ultrasound transmitter and receiver (which are typically made from piezoelectric materials). For instance, the specific impedance ratio of PZT (lead zirconate titanate) to tissue is about 20, whereas that of PZT to air is about 7×10^4 .¹⁸ Alleviating the impedance mismatch issue between PZT and tissue or water (by means of matching layers^{28,29}) is therefore an easier task than trying the same between PZT and air.

In a 2013 paper, Roes *et al.*¹⁸ reviewed the existing literature of UAET, along with a detailed account of its

^{a)}Author to whom correspondence should be addressed. Electronic mail: alper.erturk@me.gatech.edu

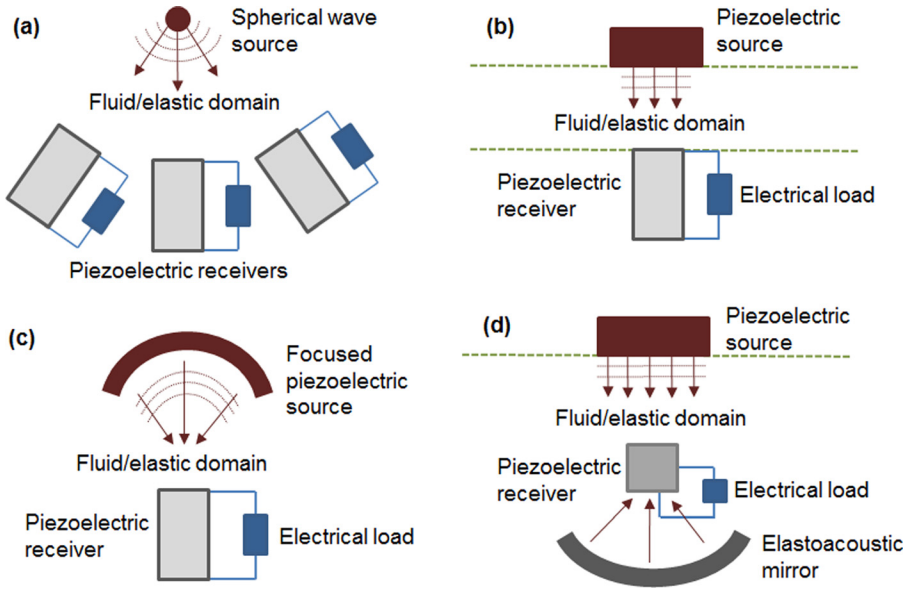


FIG. 1. Various UAET concepts using piezoelectric transduction: (a) Excitation of an array of receivers by a pulsating sphere in the same domain (e.g., powering of an underwater sensor network); (b) excitation of a receiver in a separate domain (e.g., as in transcutaneous UAET¹⁹); (c) enhanced power transfer by focusing of the source; and (d) enhanced power transfer by using a parabolic mirror at the receiver to focus plane waves (3D analog of our recent structure-borne energy harvesting concepts employing 2D elastoacoustic mirrors^{11–13}).

advantages over inductive, microwave, capacitive, and optical energy transfer methods. It is inferred from their review that the limited literature of UAET lacks fully coupled modeling efforts for the resulting multiphysics problem. To this end, the present work aims to establish and experimentally validate an analytical modeling framework that relates the incident acoustic wave originating from a source of known strength to the electrical power output extracted by a free-free piezoelectric receiver, and to report the effects of various parameters along with the optimal electrical loading conditions. Various concepts can be considered for UAET as summarized in Fig. 1, while the present work is focused on the special case of Fig. 1(a) with a single receiver (under electrical and fluid loading) excited by a spherical acoustic wave source.

II. THEORY: ACOUSTIC-PIEZOELECTRIC STRUCTURE COUPLING OF A SPHERICAL WAVE SOURCE AND A 33-MODE RECEIVER

A. Governing distributed-parameter equations

Figure 2 displays a schematic and a finite-element simulation snapshot of a piezoelectric receiver fully submerged in fluid (e.g., water) and excited by incident acoustic waves originating from a spherical source of known strength Q . The receiver is a free-free piezoelectric cylinder operating in the 33-mode of piezoelectricity (3-direction is the axial direction, i.e., ξ -axis) with a fundamental resonance frequency above the human audible frequency range. The top and bottom faces of the receiver have perfectly conductive electrodes of negligible thickness. In order to quantify the electrical power output, an external electrical load with the admittance Y_l is connected to the electrodes. (In the case of purely resistive electrical loading $Y_l = 1/R_l$, where R_l is the load resistance—note that complex conjugate loading for broadband performance is discussed elsewhere.³⁰)

For the fluid-loaded and electrically loaded free-free piezoelectric receiver bar excited by the acoustic wave, the

coupled partial differential equation for longitudinal vibrations and the AC electrical circuit equation can be derived as

$$\begin{aligned}
 -YA \frac{\partial^2 u(\xi, t)}{\partial \xi^2} - c_x \frac{\partial^3 u(\xi, t)}{\partial \xi^2 \partial t} + c_\beta \frac{\partial u(\xi, t)}{\partial t} + R_r[\delta(\xi)] \frac{\partial u(\xi, t)}{\partial t} \\
 + R_r[\delta(\xi - L)] \frac{\partial u(\xi, t)}{\partial t} + m \frac{\partial^2 u(\xi, t)}{\partial t^2} \\
 - \theta v(t)[\delta(\xi - L) - \delta(\xi)] \\
 = f_i(t)[\delta(\xi)] - f_b(t - \tau)[\delta(\xi - L)], \quad (1)
 \end{aligned}$$

$$C_p \frac{dv(t)}{dt} + Y_l v(t) + \int_0^L \theta \frac{\partial^2 u(\xi, t)}{\partial t \partial \xi} d\xi = 0, \quad (2)$$

where $u(\xi, t)$ is the displacement response of the bar at the axial position ξ and time t , $v(t)$ is the voltage output across the electrical load, Y is the Young's modulus at constant electric field, A is the cross sectional area (therefore, YA is the axial rigidity of the receiver under short-circuit condition), m is the mass per unit length, c_x is the stiffness-proportional damping coefficient, c_β is the mass-proportional

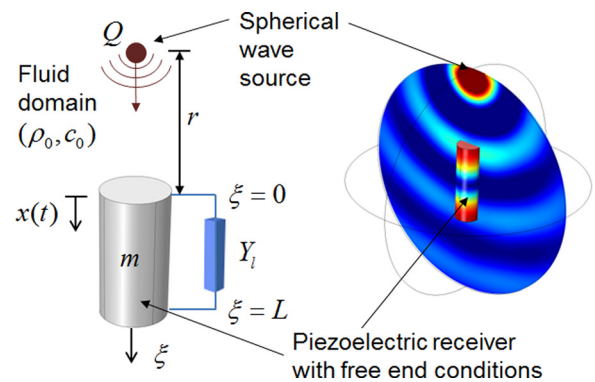


FIG. 2. Schematic representation (left) and 3D finite-element simulation snapshot (right) of contactless acoustic energy transfer from a spherical wave source to an axially poled cylindrical piezoelectric receiver bar shunted to an electrical load from its surface electrodes (which cover the top and bottom faces).

damping coefficient (c_α and c_β represent the generalized *in-vacuo* dissipation in the proportional damping form—the fluid damping is accounted for separately), θ is the electromechanical coupling term in physical coordinates, and $\delta(\xi)$ is the Dirac delta function. Furthermore, in Eq. (2), C_p and Y_l are the internal capacitance of the piezoelectric receiver and the admittance of the external load, respectively. The excitation forces due to the incident acoustic pressure are $f_i(t) = p(t)A$ at $\xi = 0$ and $f_b(t - \tau) = \mu p(t - \tau)A$ at $\xi = L$, given in terms of the acoustic pressure $p(t) = P e^{j\omega t}$ evaluated at the top surface ($\xi = 0$) and the bottom surface ($\xi = L$) of the receiver, where P is the complex pressure amplitude, ω is the excitation frequency, j is the unit imaginary number, μ is the ratio of the acoustic pressure on the bottom surface to that on the top surface, and τ is the time delay of f_b relative to f_i . (Therefore, τ depends on the wave propagation speed in fluid and the receiver length, L .) Moreover, the dissipative term R_r in Eq. (1) is the resistive component of the fluid radiation impedance³¹ (for a circular piston oscillating on one side with no baffle) defined as $R_r = \sigma_R(ka)\rho_0 c_0 A(1 - J_1(2ka)/ka)$, where J_1 is the first-order Bessel function of the first kind, $k = \omega/c_0$ is the wave number, c_0 is the speed of sound in the surrounding fluid, ρ_0 is the mass density of the surrounding fluid, a is the radius of the piston, and $\sigma_R(ka)$ accounts for the modification relative to baffled piston (see Figure 10.19 in Ref. 32).⁴² The pressure field created by a pulsating spherical harmonic wave source in an infinite, homogeneous, and isotropic medium is^{33,34} $p(t) = \rho_0 c_0 [-jkQ/4\pi r(1 - jk\bar{a})] e^{j(\omega t + k(r - \bar{a}))}$, where r is source-to-receiver distance, \bar{a} is the source radius, and Q is the acoustic source strength of the spherical wave generator (transmitter). As depicted in Fig. 2, the longitudinal strain axis and the electrical poling axis (perpendicular to the

surface electrodes) are coincident, and therefore the receiver bar is employed in the 33-mode of piezoelectricity. The dielectric loss is neglected, although it can easily be included by using a complex permittivity accounting for the loss tangent of the piezoelectric material so that C_p becomes $C_p(1 - j\delta_\epsilon)$. While the present work is focused on AC electrical output of the receiver, it is possible to account for AC-DC conversion and rectification in the circuit dynamics^{8,35,36} with a piecewise form of Eq. (2).

B. Fluid-loaded fundamental mode shape and natural frequency

The linear displacement at the free end of piezoelectric receiver bar ($x(t)$ in Fig. 2, where $x(t) = u(0, t)$) due to harmonic excitation at or around the fundamental longitudinal (axial) vibration mode is obtained by modal analysis of the distributed-parameter electromechanical system with a focus on the first mode only (i.e., higher modes are excluded in the following). The longitudinal tip displacement of the piezoelectric receiver bar at time t is then

$$x(t) = u(\xi, t)|_{\xi=0} = \phi(0)\eta(t), \quad (3)$$

where $\phi(0)$ and $\eta(t)$ are, respectively, the mass-normalized eigenfunction evaluated at $\xi = 0$ (in Fig. 2) and the generalized modal coordinate for the longitudinal vibration mode of a free-free uniform bar. The mass normalized elastic-mode eigenfunction is obtained from the corresponding undamped and electromechanically uncoupled (short-circuit) free vibration problem (which satisfies the companion mass and stiffness forms of the orthogonality conditions) is obtained as⁴³

$$\phi(\xi) = \frac{[\cos(\alpha\xi/L) - \alpha\beta \sin(\alpha\xi/L)]}{\sqrt{\int_0^L m[\cos(\alpha\xi/L) - \alpha\beta \sin(\alpha\xi/L)]^2 d\xi + m_r[\cos(\alpha) - \alpha\beta \sin(\alpha)]^2 + m_r}}. \quad (4)$$

Here, the eigenvalue (α) of the fundamental mode is the first non-zero root of the transcendental equation $(\alpha^2\beta^2 - 1)\tan\alpha - 2\alpha\beta = 0$, while the radiation mass-to-receiver mass ratio is $\beta = m_r/mL$ (where $m_r = X_r/\omega$ is the radiation mass, i.e., added mass, due to reactive component of fluid radiation impedance, $X_r = \sigma_X(ka)\rho_0 c_0 A(H_1(2ka)/ka)$, where H_1 is the Struve function of the first kind, and $\sigma_X(ka)$ is the modification relative to baffled piston (e.g., Figure 10.19 in Ref. 32)). The fundamental short-circuit natural frequency is $\omega_n = \alpha\sqrt{1/s_{33}^E\rho L^2}$ (obtained for the first non-zero eigenvalue α), where s_{33}^E is the longitudinal elastic compliance at constant electric field and ρ is the mass density of piezoelectric receiver bar.

C. Lumped-parameter form and response to harmonic excitation

The electromechanically coupled equations of forced vibration and current balance are expressed for the

fundamental mode in lumped-parameter form (reduced from distributed-parameter solution) as

$$\begin{aligned} \ddot{x}(t) + [2\zeta\omega_n + R_r\phi^2(0) + R_r\phi^2(L)]\dot{x}(t) \\ + \omega_n^2 x(t) - \theta[\phi(0)\phi(L) - \phi^2(0)]v(t) \\ = f_i(t)\phi^2(0) - f_b(t - \tau)\phi(0)\phi(L), \end{aligned} \quad (5)$$

$$C_p\phi(0)\dot{v}(t) + Y_l\phi(0)v(t) + \theta[\phi(L) - \phi(0)]\dot{x}(t) = 0. \quad (6)$$

Here, $\phi(0)$ and $\phi(L)$ are, respectively, the mass-normalized fundamental elastic mode eigenfunction evaluated at $\xi = 0$ and $\xi = L$ (in Fig. 2) for the longitudinal vibration mode of a free-free uniform fully submerged bar (Eq. (4)), and an overdot represents differentiation with respect to time. Fluid absorption and scattering effects on the incident pressure are assumed to be negligible for the frequency range of interest and receiver dimensions (confirmed with the experiments).

The steady-state electromechanical response to harmonic excitation is also harmonic and is of the form $x(t) = Xe^{j\omega t}$ and $v(t) = Ve^{j\omega t}$ based on the linear system

$$\frac{v(t)}{Qe^{j(\omega t + k(r-\bar{a}))}} = \frac{j\omega\theta \left(\rho_0 c_0 A \frac{jk}{4\pi r(1-jk\bar{a})} \right) [\phi(0) - \mu\phi(L)e^{-j\varphi}] [\phi(L) - \phi(0)]}{\left\{ \omega_n^2 - \omega^2 + j\omega [2\zeta\omega_n + R_r [\phi^2(0) + \phi^2(L)]] \right\} (Y_l(\omega) + j\omega C_p) + j\omega\theta^2 [\phi(L) - \phi(0)]^2}, \quad (7)$$

where $\varphi = \omega\tau$ is the phase angle between the excitation forces at the top and bottom surfaces of the cylindrical receiver.

D. Electromechanical impedance of the fluid-loaded receiver

Deriving an expression for the impedance of the fluid-loaded receiver is useful for identification of its parameters under electrical excitation. In Eq. (5), changing the input to $v(t) = Ve^{j\omega t}$ and setting $f_i(t) = f_b(t - \tau) = 0$, while in Eq. (6), replacing the current output $Y_I v(t)$ by the actuation current input $-i(t) = -Ie^{j\omega t}$, yields the following expression for the fluid-loaded receiver's electromechanical impedance $Z = V/I$:

$$Z(\omega) = \left\{ j\omega \left[C_p + \frac{\theta^2 [\phi(L) - \phi(0)]^2}{\omega_n^2 - \omega^2 + j\omega [2\zeta\omega_n + R_r \phi^2(0) + R_r \phi^2(L)]} \right] \right\}^{-1}, \quad (8)$$

which includes the fundamental longitudinal vibration mode only.

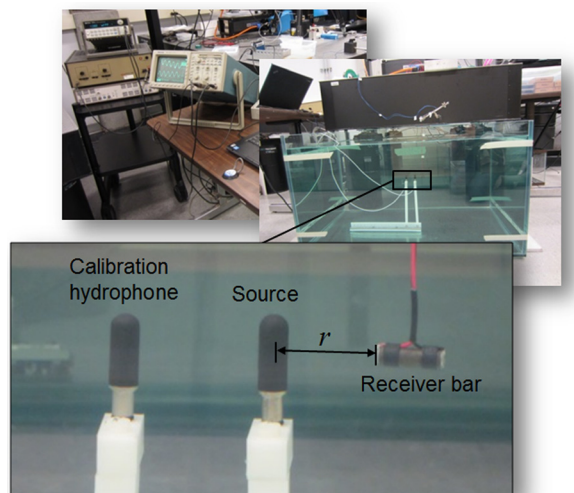


FIG. 3. Experimental setup and close-up pictures showing the source (transmitter) and the receiver bar submerged in tap water.

assumption. Then the fundamental-mode voltage output per source strength frequency response function (FRF) can be obtained as

III. EXPERIMENTAL RESULTS AND MODEL VALIDATION

A. Experimental setup and fluid-loaded receiver impedance

Experiments are conducted for an axially poled monolithic cylindrical piezoelectric bar (modified PZT from PI Ceramic GmbH) of length $L = 20$ mm and radius $a = 3$ mm, which is employed as the receiver (Fig. 3). The receiver has silver electrodes covering its top and bottom faces. For the experimental configuration, orientation, and receiver dimensions in Fig. 3, the hydrophone (B&K 8103) employed in reverse operation as a source is a reasonable representation of a spherical source for model validation. The incident pressure field $p(t)$ at the leading surface of the receiver) can be obtained from an experiment (in a water tank) through pressure-to-source strength correlation in frequency domain for an open-loop burst signal from a projector to a hydrophone. Hence, by means of a second hydrophone used for calibration, the acoustic strength of the source is extracted using $Q = p(r)(-2j\lambda r)/\rho_0 c_0$, where $p(r)$ is the pressure at distance r from the projector and λ is the acoustic wavelength in fluid.

The receiver is coated with a thin layer of electrically insulating, acoustically transparent material to avoid shorting under water. The analytical and experimental impedance FRFs for in-air and underwater actuation are shown in Fig. 4. The impedance measurement captures the fundamental resonance and anti-resonance frequencies of the receiver bar, which are also called the short- and open-circuit resonance frequencies, and they have the values of 75 kHz and

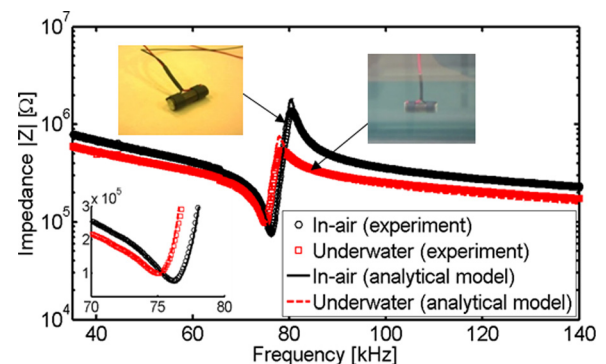


FIG. 4. In-air and underwater electromechanical impedance FRFs of the piezoelectric receiver bar in free-free boundary conditions showing the agreement between experimental data and model prediction.

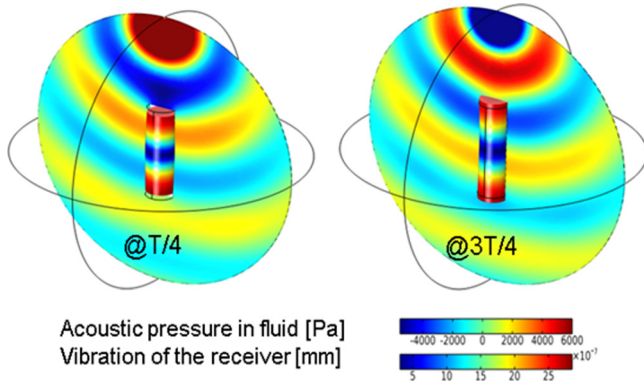


FIG. 5. Finite-element simulation for spherical acoustic wave excitation of the free-free piezoelectric receiver bar in water with a focus on the acoustic pressure field in fluid and the vibration (displacement) field of the receiver at two instants of one period (T) at the fundamental open-circuit resonance frequency (79 kHz).

79 kHz, respectively. Added mass and damping effects due to water loading are clearly observed in Fig. 4, and the model successfully represents the underwater dynamics of the receiver near resonance. It should be noted that the resistive and reactive components of the radiation impedance determine the fluid-induced damping and fluid-loaded resonance frequency, and they depend on the dimensions (e.g., diameter) of the receiver (as a design parameter). The model was evaluated using receiver parameters of $s_{33}^E = 14.2 \text{ pm}^2/\text{N}$, $\rho = 7800 \text{ kg/m}^3$, $C_p = 5.5 \text{ pF}$, $\theta = 0.0085 \text{ C/m}$, and $\zeta = 0.01$, and with water parameters $\rho_0 = 1000 \text{ kg/m}^3$ and estimated^{32,37} $c_0 = 1490.5 \text{ m/s}$. It is expected that the identified in-air damping ratio ($\zeta = 0.01$) is dominated by the material loss. Therefore, we use this as an approximation to *in-vacuo* damping. Fluid damping in the underwater case is taken into account by the model as described in Sec. II.⁴⁴

B. Finite-element vs. analytical model simulations

Multiphysics finite-element simulations are performed in COMSOL to explore the 3D behavior of the receiver and fluid (water) under harmonic excitation. The relevant simulation tool in finite-element modeling is limited to open-circuit conditions unless it is coupled with a circuit simulator tool. Acoustic waves excite the free-free piezoelectric bar submerged in fluid domain, and boundaries of the fluid domain are defined to allow no reflection. For excitation at the fundamental open-circuit resonance frequency (79 kHz), Fig. 5 shows the acoustic pressure field in fluid domain and longitudinal displacement field in the receiver bar at two instants of the period (T) of excitation for the extreme compressive and tensile deformations of the receiver during a cycle of harmonic excitation.

In Figs. 6(a) and 6(b), the longitudinal tip displacement (at $\xi = 0$ in Fig. 2) and open-circuit voltage output FRFs are extracted and plotted using the finite-element and the analytical models. Very good agreement is observed between 3D finite-element simulations and the proposed analytical multiphysics model. Since the default version of the finite-element software is limited to open-circuit simulations, comparisons of frequency-domain analytical and time-domain numerical

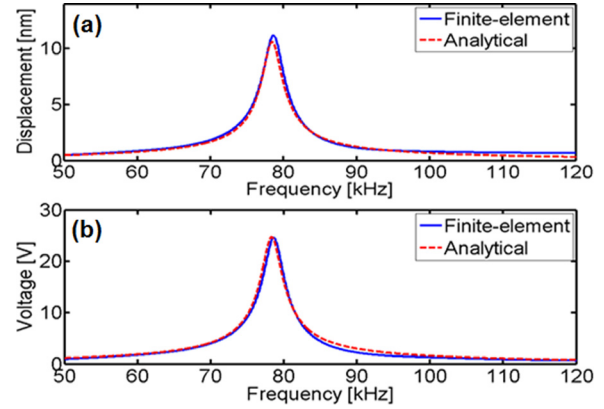


FIG. 6. Finite-element vs. analytical model simulations of the open-circuit (a) tip displacement and (b) voltage output FRFs (for $Q = 5.65 \mu\text{m}^3/\text{s}$, $a = 3 \text{ mm}$, and $r = 30 \text{ mm}$).

simulations will be limited to open-circuit electrical boundary conditions. However, the analytical model can easily accommodate the addition of a finite electrical load impedance, as discussed next prior to the experimental validations.

Using the analytical model, further simulations are conducted for a broad range of resistive electrical load R_l (such that $Y_l = 1/R_l$ in Eq. (2)) and excitation frequency values to extract the optimality conditions of the receiver. The source-to-receiver distance $r = 30.2 \text{ mm}$ is based on the identified experimental value as a preliminary analysis for Sec. III C. Using Eq. (7) in the power expression $\Pi = v^2/R_l$, the power output FRF normalized with source strength squared (Π/Q^2) is calculated, and plotted versus frequency in Fig. 7 (note that $\Pi \propto Q^2$, since $v \propto Q$). In agreement with typical piezoelectric energy harvesting problems,³⁵ two peaks of power output are observed at the fundamental short- and open-circuit resonance frequencies. The first peak gives the local maximum power at 75 kHz as $0.0294 \text{ mW}/(\text{cm}^3/\text{s})^2$ for the optimal electrical load of $150 \text{ k}\Omega$, while the second and the global peak at 79 kHz is $0.0314 \text{ mW}/(\text{cm}^3/\text{s})^2$ for the optimal load of $1.5 \text{ M}\Omega$. The peak power outputs at the short- and open-circuit resonance frequencies are not identical since the receiver is not very lightly damped especially in the presence of fluid effects;³⁰ nevertheless, they are relatively similar. Therefore, a lower matched electrical load resistance is achieved at 75 kHz with larger current, whereas the opposite

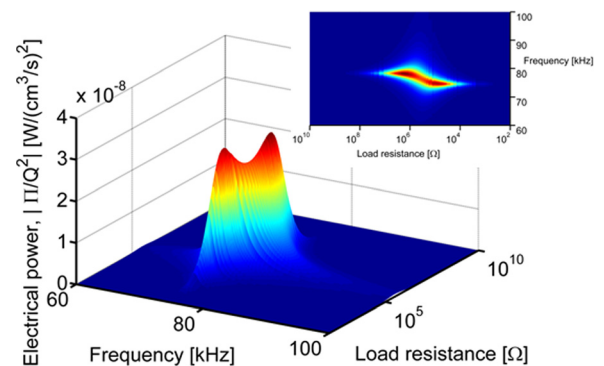


FIG. 7. Power output (normalized with respect to source strength squared) for the piezoelectric receiver vs. excitation frequency and load resistance simulated by using the analytical model (for $r = 30.2 \text{ mm}$).

(larger optimal load with lower current) is the case at 79 kHz.

C. Experimental results and analytical model validation

Experiments are performed to excite the free-free receiver bar as shown in Fig. 3 for validating the analytical model and to gain a detailed understanding of the coupled system dynamics. The acoustic excitation source is a hydrophone (under reverse operation as a source) and the receiver is the free-free cylindrical piezoelectric bar operating in 33-mode of piezoelectricity and shunted to an electrical load as described previously and characterized in Fig. 4. For the geometric alignment, distance, and frequencies used in the experiments, the experimental source device behaves as a spherical source. The strength of the source transducer under open-loop voltage excitation is calibrated with a separate hydrophone, itself calibrated using reciprocity.³⁸ In all cases, the source is excited by sinusoidal burst (3 cycles) at selected frequencies by means of a function generator and amplifier. Burst excitation is preferred to continuous excitation to properly track the signal and avoid excitation of the receiver by undesired reflections (although the water tank used in the experiments is sufficiently large). The electrodes of the piezoelectric receiver bar are shunted to a resistance substitution box, and the voltage output is recorded by the data acquisition system. In the following, the Fast Fourier Transform (FFT) of the burst excitation originating from the source is used in conjunction with the voltage FRF given by Eq. (7) to eventually obtain the inverse FFT of the voltage output for each resistive load.

Typical time histories of the voltage output across the electrical load connected to the receiver bar are shown in Fig. 8 in response to 3-cycle burst excitations at two different frequencies (fundamental short- and open-circuit resonance frequencies) as the two separate cases. In the experiments corresponding to this figure, the receiver is located at $r = 30.2$ mm and an electrical load of $R_l = 1.5$ M Ω is applied. The distance between the source and the receiver is

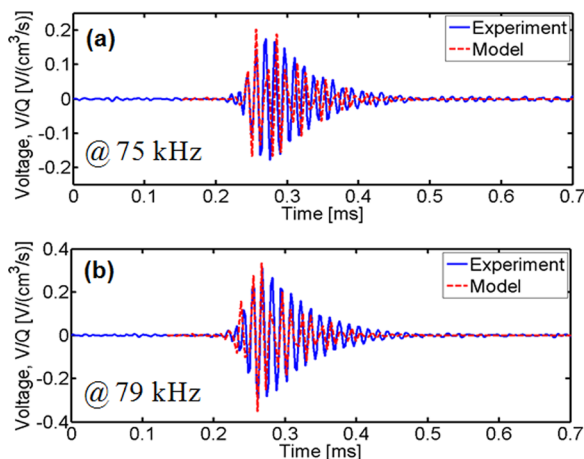


FIG. 8. Voltage response of the receiver to 3-cycle burst excitations at the fundamental (a) short-circuit and (b) open-circuit resonance frequencies of 75 kHz and 79 kHz (for a source-to-receiver distance of $r = 30.2$ mm and load resistance of $R_l = 1.5$ M Ω).

extracted using the delay of approximately 20.3 μ s between their time signals and the estimated speed of sound, 1490.5 m/s. The two graphs in Fig. 8 show both experimental measurements and model predictions of the response histories for excitations at 75 kHz and 79 kHz, respectively. By keeping the load resistance at $R_l = 1.5$ M Ω , burst excitations are performed at different frequencies. The resulting root-mean-square voltage output and average power output FRFs over a broad range of excitation frequencies are shown in Fig. 9. Clearly, for this electrical load resistance value, the maximum power output takes place around 79 kHz, in agreement with Fig. 7. Very good agreement is observed between the model predictions and experimental measurements in Figs. 8 and 9.

D. Effects of various system parameters

Next, resistor sweep experiments are performed for 3-cycle burst excitations at the fundamental short- and open-circuit resonance frequencies while keeping the source-to-receiver distance fixed (at $r = 30.2$ mm). The tests are conducted for a set of load resistance values ranging from 100 k Ω to 9 M Ω , covering a broad range that is expected to include the optimal loads at 75 kHz and 79 kHz. As shown in Fig. 10(a), very good agreement is observed between experimental data and analytical model predictions of the power output normalized with respect to source strength squared. The load resistance is then fixed to $R_l = 1.5$ M Ω , and the effect of source-to-receiver distance is studied as given in Fig. 10(b). The hyperbolic dependence of the power output to distance is expected since $v_{rms} \propto 1/r$ in Eq. (7), and therefore, $\Pi_{avg} = v_{rms}^2/R_l \propto 1/r^2$ for a fixed Q_{rms} value. With increased source-to-receiver distance, the power output of the receiver decreases monotonically. Finally, the dependence of the average power output on the root-mean-square

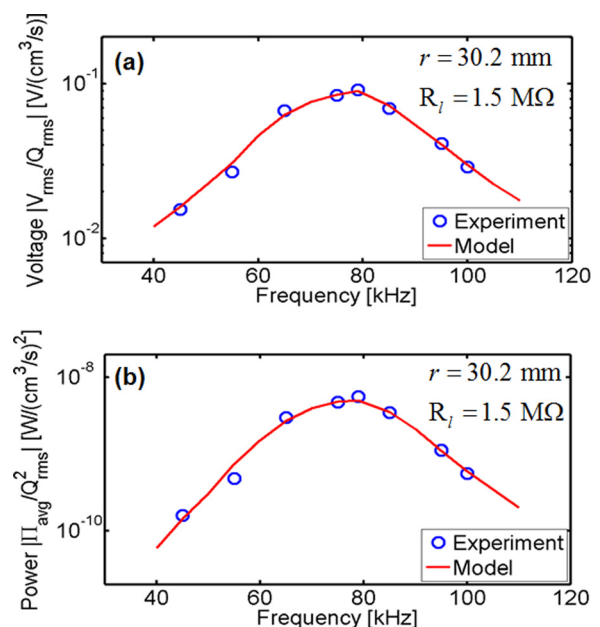


FIG. 9. Root-mean-square (a) voltage output and (b) average power output FRFs of the receiver normalized with respect to source strength (for a source-to-receiver distance of $r = 30.2$ mm and load resistance of $R_l = 1.5$ M Ω).

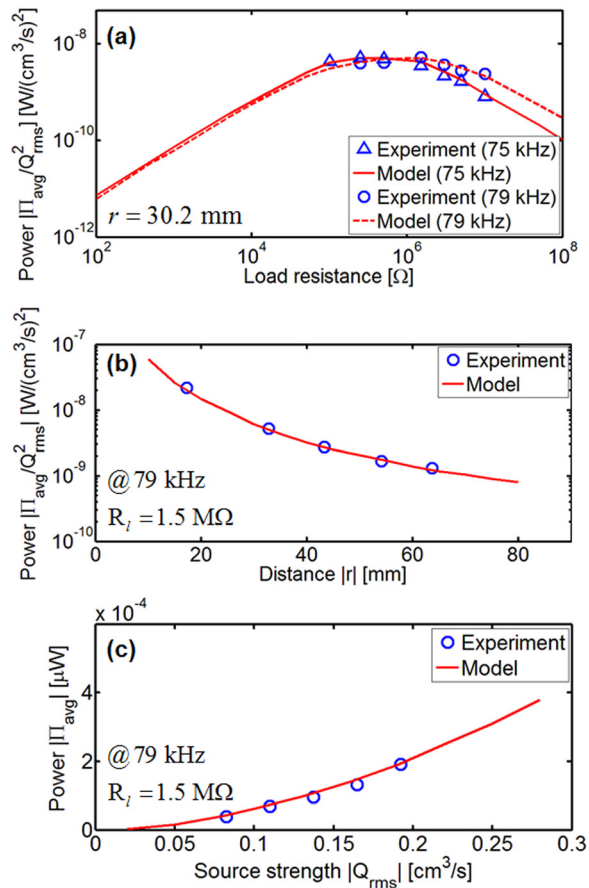


FIG. 10. (a) Power output (normalized with respect to source strength squared) vs. electrical load resistance at the fundamental underwater short- and open-circuit resonance frequencies (for $r = 30.2$ mm); (b) power output (normalized with respect to source strength squared) vs. source-to-receiver distance (for $R_l = 1.5$ M Ω excitation at 79 kHz); (c) power output vs. source strength (for $R_l = 1.5$ M Ω excitation at 79 kHz).

source strength is displayed in Fig. 10(c), validating the previously mentioned quadratic relationship $\Pi_{\text{avg}} \propto Q_{\text{rms}}^2$ with good accuracy.

IV. CONCLUSIONS

Contactless power transfer is of interest for wireless applications ranging from medical deep implants to sensors located in hazardous environments for which battery replacement or tethered charging is either undesirable or impossible. As an alternative to the well-studied inductive (near-field electromagnetic) coupling method, the use of ultrasonic acoustic waves for contactless power transfer has received growing attention due to various advantages offered by the latter approach, such as increased source-to-receiver distance, elimination of electromagnetic fields, and frequency-wise flexibility. While proof-of-concept experiments demonstrate the feasibility of this approach; from the standpoint of system-level modeling and multiphysics understanding, the field of ultrasonic acoustic energy transfer is still in its infancy as pointed out in the recent literature. In this paper, contactless ultrasonic acoustic energy transfer is investigated analytically, numerically, and experimentally for a cylindrical receiver in free-free

mechanical boundary conditions excited by a spherical wave source. Specifically, a fully coupled multiphysics analytical model (that accounts for the acoustic-piezoelectric structure interaction and the fluid-loaded receiver's electrical load) is developed and successfully validated. Optimal electrical loading conditions are shown and experimentally validated to be at the fundamental short- and open-circuit resonance frequencies of the receiver bar, which are associated with larger current and larger voltage, respectively, yielding similar power outputs. Effects of various system parameters, such as the source strength and the source-to-receiver distance, are also presented and validated. Future research directions include focusing of the excitation as in high intensity focused ultrasound configurations with curved transducers,³⁹ or by using proper mirroring concepts,^{11–13} (as well as resulting acoustic⁴⁰ and transducer⁴¹ nonlinearities) in addition to exploring and alleviating impedance mismatch issues^{28,29} in problems that necessarily involve multiple domains.¹⁹

- ¹K. Cook-Chennault, N. Thambi, and A. Sastry, *Smart Mater. Struct.* **17**(4), 043001 (2008).
- ²N. S. Hudak and G. G. Amatucci, *J. Appl. Phys.* **103**(10), 101301 (2008).
- ³M. I. Friswell and S. Adhikari, *J. Appl. Phys.* **108**(1), 014901 (2010).
- ⁴S. Ali, S. Adhikari, M. Friswell, and S. Narayanan, *J. Appl. Phys.* **109**(7), 074904 (2011).
- ⁵A. Giacomello and M. Porfiri, *J. Appl. Phys.* **109**(8), 084903 (2011).
- ⁶L. Tang and Y. Yang, *Appl. Phys. Lett.* **101**(9), 094102 (2012).
- ⁷C. K. Kwiimy, G. Litak, M. Borowiec, and C. Nataraj, *Appl. Phys. Lett.* **100**(2), 024103 (2012).
- ⁸N. Elvin and A. Erturk, *Advances in Energy Harvesting Methods* (Springer, 2013).
- ⁹M. Lallart, L. Wang, C. Richard, L. Petit, and D. Guyomar, *J. Appl. Phys.* **116**(12), 124106 (2014).
- ¹⁰O. Goushcha, N. Elvin, and Y. Andreopoulos, *Appl. Phys. Lett.* **104**(2), 021919 (2014).
- ¹¹M. Carrara, M. Cacan, M. Leamy, M. Ruzzene, and A. Erturk, *Appl. Phys. Lett.* **100**(20), 204105 (2012).
- ¹²M. Carrara, M. Cacan, J. Toussaint, M. Leamy, M. Ruzzene, and A. Erturk, *Smart Mater. Struct.* **22**(6), 065004 (2013).
- ¹³M. Carrara, J. Kulpe, S. Leadenham, M. Leamy, and A. Erturk, *Appl. Phys. Lett.* **106**(1), 013907 (2015).
- ¹⁴X. Yu, S. Sandhu, S. Beiker, R. Sassoon, and S. Fan, *Appl. Phys. Lett.* **99**(21), 214102 (2011).
- ¹⁵S. Kim, J. S. Ho, L. Y. Chen, and A. S. Poon, *Appl. Phys. Lett.* **101**(7), 073701 (2012).
- ¹⁶Z. Zhang, K. Chau, C. Liu, C. Qiu, and F. Lin, *J. Appl. Phys.* **115**(17), 17A328 (2014).
- ¹⁷A. Kurs, A. Karalis, R. Moffatt, J. D. Joannopoulos, P. Fisher, and M. Soljačić, *Science* **317**(5834), 83–86 (2007).
- ¹⁸M. G. L. Roes, J. L. Duarte, A. M. Hendrix, and E. A. Lomonova, *IEEE Trans. Ind. Electron.* **60**(1), 242 (2013).
- ¹⁹S. Ozeri and D. Shmilovitz, *Ultrasonics* **50**(6), 556–566 (2010).
- ²⁰A. Denisov and E. Yeatman, in *Proceedings of the International Conference on Body Sensor Networks (BSN)* (IEEE, Singapore, 2010), pp. 84–89.
- ²¹A. Denisov and E. Yeatman, in *Proceedings of the 2013 IEEE International Conference on Body Sensor Networks (BSN)* (IEEE, Cambridge, MA, 2013), pp. 1–5.
- ²²E. Yeatman and P. Mitcheson, in *Body Sensor Networks* (Springer, 2014), pp. 237–272.
- ²³G. V. Cochran, M. Johnson, M. Kadaba, F. Vosburgh, M. Ferguson-Pell, and V. Palmeiri, *J. Orthop. Res.* **3**(4), 508–513 (1985).
- ²⁴G. V. Cochran, M. P. Kadaba, and V. R. Palmieri, *J. Orthop. Res.* **6**(1), 145–147 (1988).
- ²⁵H. Kawanabe, T. Katane, H. Saotome, O. Saito, and K. Kobayashi, *Jpn. J. Appl. Phys., Part 1* **40**, 3865 (2001).
- ²⁶S.-n. Suzuki, S. Kimura, T. Katane, H. Saotome, O. Saito, and K. Kobayashi, *Jpn. J. Appl. Phys., Part 1* **41**(5B), 3600–3603 (2002).

- ²⁷T. Maleki, N. Cao, S. H. Song, C. Kao, S.-C. Ko, and B. Ziaie, *IEEE Trans. Biomed. Eng.* **58**(11), 3104–3111 (2011).
- ²⁸J. H. Goll and B. A. Auld, *IEEE Trans. Son. Ultrason.* **22**(1), 52–53 (1975).
- ²⁹H. Persson and C. Hertz, *Ultrasonics* **23**(2), 83–89 (1985).
- ³⁰S. Shahab and A. Erturk, *Smart Mater. Struct.* **23**(12), 125032 (2014).
- ³¹L. E. Kinsler, A. R. Frey, A. B. Coppens, and J. V. Sanders, *Fundamentals of Acoustics* (Wiley–VCH, 1999).
- ³²C. H. Sherman and J. L. Butler, *Transducers and Arrays for Underwater Sound* (Springer, 2007).
- ³³A. D. Pierce, *Acoustics: An Introduction to Its Physical Principles and Applications* (Acoustical Soc of America, 1989).
- ³⁴D. A. Russell, J. P. Titlow, and Y.-J. Bemmen, *Am. J. Phys.* **67**(8), 660–664 (1999).
- ³⁵A. Erturk and D. J. Inman, *Piezoelectric Energy Harvesting* (Wiley, Chichester, UK, 2011).
- ³⁶C. J. Rupp, M. L. Dunn, and K. Maute, *J. Intell. Mater. Syst. Struct.* **21**(14), 1383–1396 (2010).
- ³⁷C. T. Chen and F. J. Millero, *J. Acoust. Soc. Am.* **62**(5), 1129–1135 (1977).
- ³⁸L. Luker and A. Van Buren, *J. Acoust. Soc. Am.* **70**(2), 516–519 (1981).
- ³⁹M. S. Canney, M. R. Bailey, L. A. Crum, V. A. Khokhlova, and O. A. Sapozhnikov, *J. Acoust. Soc. Am.* **124**(4), 2406–2420 (2008).
- ⁴⁰M. F. Hamilton and D. T. Blackstock, *Nonlinear Acoustics* (Academic press, San Diego, 1998).
- ⁴¹S. Leadenham and A. Erturk, *Nonlinear Dyn.* **79**, 1727–1743 (2015).
- ⁴²Therefore, the added damping due to fluid loading is directly given in Eq. (1), whereas the added mass at the free ends is to be accounted for as boundary conditions.
- ⁴³Note that the rigid-body mode resulting from the positive semi-definite nature of the system (with free-free boundary conditions) is not of interest.
- ⁴⁴For the case of a very high mechanical quality factor receiver (such that $\zeta \sim 0.001$), which is preferred for larger power output, the total underwater damping would be dominated by the fluid (acoustic radiation) damping. That is, even for the extreme of $\zeta \rightarrow 0$ the underwater response would be bounded due to fluid damping.